

Non-Zeeman Circular Polarization of Molecular Spectral Lines in the ISM

Mohammed Afif Chamma

May 8, 2018

Submitted in partial fulfillment
of the requirements for the degree
of M.Sc. Astronomy

Supervised by Dr. Martin Houde
Department of Physics and Astronomy
University of Western Ontario
London, Ontario, Canada

Co-Authorship

The archival data that forms the basis of this work was reduced and provided by Dr. Ramprasad Rao, receiver engineer at the Submillimeter Array (SMA) on Mauna Kea. The idea for and first version of the code that performs the correction necessary to eliminate false signals was provided by Dr. Josep Miquel Girart, who was visiting the SMA at the same time as I was. My supervisor, Dr. Martin Houde, provided extensive edits on several drafts of this paper and guidance on how to coax out the signals from the noise and display them in a clear way.

As for my role, I adapted Dr. Girart's code and used it to correct the archival data provided by Dr. Rao for four different astronomical objects. I created software built on top of the reduction package *Miriad* to efficiently collect data for and create the many figures and maps required to make the case that the signals we were presenting were true signals. Dr. Houde and I interpreted the data and detailed the arguments present in the paper to support the reliability of the signals. I was responsible for writing drafts of the paper and this report.

Contents

1	Introduction	4
1.1	Magnetic Fields through Polarimetry	6
2	Research Methods	7
2.1	Radio Interferometry	8
2.2	Data Reduction with <i>Miriad</i>	12
2.3	Code Repositories	17
3	Acknowledgements	18
4	References	19

1 Introduction

Stars form when clouds of gas and dust collapse gravitationally until they are hot enough to ignite fusion in their core. Assuming that gravity is the dominant force in the star formation process one can calculate several parameters such as the maximum mass stable to gravitational collapse (the Jeans mass), and the free-fall timescale for such a collapse. However, the presence of turbulence and magnetic fields in a molecular cloud complicates star formation, either by slowing down the collapse or preventing it from happening at all. Developing methods of measuring and characterizing turbulence and magnetic fields in molecular clouds is an important research focus in star formation. This report focuses on polarimetry, the dominant method for measuring the magnetic field.

The magnetic field in a molecular cloud can provide support against gravitational collapse, and the strength of the field can determine the timescale at which collapse happens. The critical mass of a cloud is

$$M_\Phi = \frac{\Phi}{2\pi\sqrt{G}}, \quad (1)$$

where Φ is the magnetic flux in the cloud (Nakano & Nakamura, 1978; Crutcher, 2012). Clouds with masses below this mass are called subcritical and are supported against collapse by the magnetic field, while clouds with a mass higher than M_Φ will collapse and form stars (Nakano & Nakamura, 1978; Crutcher, 2012). In clouds that are subcritical ions are locked to the magnetic field lines and only neutral dust and gas can collapse into the core of the cloud, eventually causing the mass to increase and become supercritical (Crutcher, 2012). In clouds with weak fields the mass is already supercritical and turbulence plays a larger role in driving collapse (Crutcher, 2012).

These theoretical models make several observable predictions. The simplest is

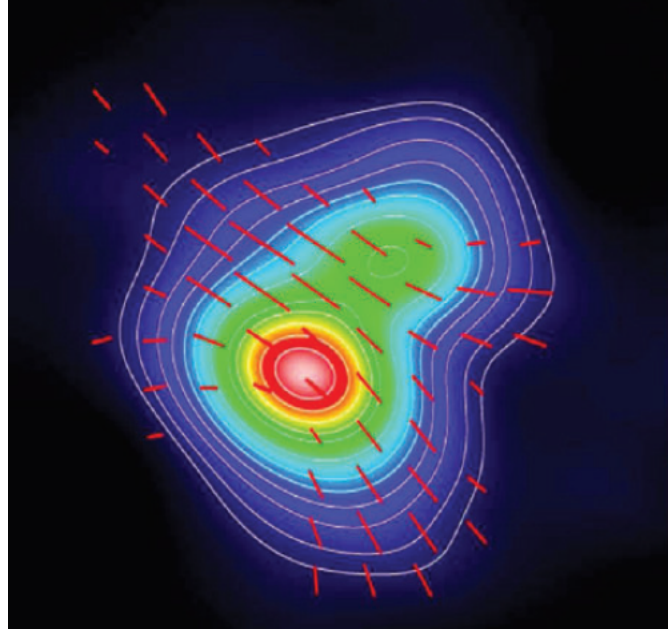


Figure 1: A map of NGC1333 IRAS4A made with the Submillimeter Array (SMA). Colours and contours show continuum dust emission, red vectors show the magnetic field in the plane of the sky (Girart, Rao, & Marrone, 2006)

that regions with strong fields will have smooth field lines throughout all stages of the cloud’s collapse (Crutcher, 2012). Collapsing clouds that are supported by strong magnetic fields will form oblate spheroids since the cloud has more support along the direction perpendicular to the field, which should be observable (Crutcher, 2012). In addition, a region with initially parallel field lines will begin to “pinch” as the cloud collapses, creating a very beautiful hourglass morphology (Crutcher, 2012). An example of this hourglass can be seen in Figure 1.

Understanding the details of the star formation process are a strong reason for developing the methodology of measuring magnetic fields around star forming regions and the interstellar medium. In astronomy, new tools for observing the universe frequently reveal surprising results and open doors into future fields, and this methodology is no exception.

1.1 Magnetic Fields through Polarimetry

Maps of the magnetic field like that shown in Figure 1 are made by measuring the polarization state of the light incident on a telescope. Inferring the magnetic field from the measured polarization state is usually done either through broadband measurements of continuum thermal emission from dust or using rotational transitions of molecules, like CO. Measuring molecular transitions has the advantage of higher intensities compared to measuring thermal dust emission. In addition, by selecting different molecules we can obtain tomographic information and more detail about the structure of the cloud. This section will give a brief overview of the two methods and gives context to certain challenges with polarimetry on molecular spectral lines that the work presented here highlights.

The mechanisms that give rise to polarized light in dust versus in molecules though both different, are related to the strength of the magnetic field in the environment. Dust grains will align themselves perpendicular to the magnetic field due to asymmetric radiative torques, causing any thermal emission from long grains to be linearly polarized perpendicular to the field (source?). Molecules interact with the magnetic field and through the Goldreich-Kylafis (GK) effect can emit a small percentage of radiation that is linearly polarized either perpendicular or parallel to the plane of the sky component of the magnetic field (Goldreich & Kylafis, 1981). The degeneracy in the direction of the magnetic field is usually resolved by measuring continuum emission along with molecular emission.

The stronger the magnetic field is in a region the stronger the alignment is of dust and molecules with the field. Therefore if we see a large dispersion in polarization angles (PAs) in a region then we might conclude that the field is weaker compared to a region where the PAs are more uniform. This idea is formally expressed by the Davis-Chandrasekhar-Fermi (DCF) method where the measured dispersion of PAs can be used to calculate a value for the plane of the sky component of the magnetic

field according to

$$B_{POS} = \sqrt{4\pi\rho} \frac{\delta V}{\delta\phi}, \quad (2)$$

where ρ is the gas density, δV is the velocity dispersion (what's that? the bandwidth?) and $\delta\phi$ is the dispersion in PAs (Davis, 1951; Chandrasekhar & Fermi, 1953; Crutcher, 2012). This method has proven useful and has seen several extensions and refinements in recent years (Hildebrand et al., 2009; Houde et al., 2009).

Since the PA is the critical piece of information that connects polarization measurements to the strength of the magnetic field, any effects that reduce the polarization percentage or rotate the PA will taint the measurement of the magnetic field. Two important examples of this that concern this report are the presence of polarized light due to the telescope's instrumentation (e.g. see Hamaker et al., 1996; Sault et al., 1996; Marrone et al., 2008) and anisotropic resonant scattering (ARS) from molecular transitions, which in principle converts linear polarization (LP) to circular polarization (CP) along the line of sight (Houde et al., 2013; Hezareh et al., 2013). Since it may be possible to retrieve the 'lost' LP by measuring CP (Hezareh et al., 2013), and the ARS effect is a common occurrence in molecular clouds (this work), measuring CP simultaneously with LP when doing molecular spectral line polarimetry may be essential to obtaining accurate measurements of the magnetic field.

2 Research Methods

The data presented in the attached paper were collected from the archive of the Submillimeter Array (SMA), an array of eight 6m radio telescopes located at Mauna Kea, Hawaii. This section will describe the basic principles of radio interferometry, how polarimetric data is collected with the SMA, and an overview of the data reduction process using the *Miriad* data reduction package (Sault et al., 1995).

2.1 Radio Interferometry

Radio interferometry is a technique for obtaining high-resolution maps of objects in the sky that avoids building gigantic primary reflectors and relies on computationally intensive data analysis tasks.

Since the resolution of a telescope goes as $\theta \propto \lambda/D$, where D is the diameter of the primary reflector, we try to build larger and larger mirrors and dishes to obtain higher resolution. However, large enough reflectors become very challenging to build when seeking resolutions of $< 1''$ at radio wavelengths. To illustrate how we can attain a higher resolution without building a massive reflector, consider a dish with a diameter 500m across: this dish gives us high resolution but is beyond our ability to manufacture. Imagine now that we remove or obstruct large sections of this reflector. The images we would obtain from such a “patchy” reflector are now in fact the Fourier transform of the intensity map of the object being examined on the sky, much like how the support struts on, for example, Hubble cause imaged stars appear to have a superimposed cross pattern. With radio interferometry, we obtain the resolution of a large dish by sampling the light it would receive and inferring the true sky image from the measured Fourier transform.

The resolution of the interferometer array is determined by the longest baseline separation B_{max} between any two elements of the array. This B_{max} is effectively the diameter of our “patchy” reflector. However while the resolution defines the scale of the smallest object that is resolvable an interferometer also has a limit on the largest resolvable object, which is defined by the shortest baseline B_{min} of any two elements in the array.

The output of a radio interferometer is the visibility function $\mathcal{V}(u, v)$, which is found by correlating the voltage signals from a pair of antennae. This correlation is done on-the-fly by an onsite computer called the correlator and the raw voltage signals are often discarded after the correlation is found due to the prohibitively large

amount of data. The arguments u and v are the distances between the two antennae Δx and Δy , respectively. Given antennae a and b the visibility is written as

$$\mathcal{V}(u, v) = \frac{\langle V_a(t) \star V_b(t) \rangle}{A_0 \Delta \nu}, \quad (3)$$

where $V_a(t)$ and $V_b(t)$ is the measured voltage signal from antennae a and b , A_0 is the collecting area of the dish, $\Delta \nu$ is the bandwidth of the receiver, and $\langle V_a(t) \star V_b(t) \rangle$ denotes the time-averaged cross-correlation of the voltage signals, which is defined by

$$\langle V_a(t) \star V_b(t) \rangle = \lim_{T \rightarrow \infty} \frac{1}{2T} \int_{-T}^T V_a(t) V_b^*(t - \tau) dt. \quad (4)$$

Here τ is a delay parameter that is chosen based on the type of observations being made (Thompson et al., 2001).

The expression shown in eq. (3) can be shown to be equivalent to the Fourier transform of the intensity map (the image) $I(l, m)$, where l and m are angular positions, through the van Cittert-Zernicke theorem. In its most general form the van Cittert-Zernicke theorem proves that incoherent radiation observed from a large distance appears to be coherent (see chap. 14 of Thompson et al., 2001, for a derivation). Here we prove a consequence of it as it relates to interferometry to show that $\mathcal{V}(u, v) = \mathcal{F}\{I(l, m)\}$, where $\mathcal{F}\{\}$ denotes the Fourier transform.

Consider two antennae a and b at positions (x_a, y_a) and (x_b, y_b) , pointed at the same object. The electric field at antennae a and b from sky position (l, m) at time t is given by

$$E_a(l, m, t) = A(l, m, t) e^{i\phi(l, m, t) + 2\pi i(x_a l + y_a m)}, \quad (5)$$

$$E_b(l, m, t) = A(l, m, t) e^{i\phi(l, m, t) + 2\pi i(x_b l + y_b m)}, \quad (6)$$

where $A(l, m, t)$ is the amplitude of the field and $\phi(l, m, t)$ is the phase of the wave

which van Cittert-Zernicke tells us is the same in both $E_a(l, m, t)$ and $E_b(l, m, t)$ since the waves are coherent. The total voltage response of the antenna's receiver is the superposition of all electromagnetic waves from each position of the object, which can be written as:

$$V_a(t) = \int \int E_a(l, m, t) dl dm, \quad (7)$$

$$V_b(t) = \int \int E_b(l, m, t) dl dm, \quad (8)$$

so the complex product is

$$\begin{aligned} V_a(t) \star V_b(t) &= \int_{l,m} E_a(l, m, t) dl dm \times \int_{l,m} E_b^*(l, m, t) dl dm \\ &= \int_{l,m} \int_{l',m'} A(l, m, t) A^*(l', m', t) e^{i\phi(l,m,t)+2\pi i(x_a l + y_a m)} \\ &\quad e^{-i\phi(l',m',t)-2\pi i(x_b l' + y_b m')} dl dm dl' dm' \\ &= \int_{l,m} A(l, m, t) A^*(l, m, t) e^{2\pi i(\Delta xl + \Delta ym)} dl dm, \end{aligned} \quad (9)$$

where the last line follows since the integral is 0 unless $\phi(l, m, t) = \phi(l', m', t)$. The positional arguments become $\Delta x \equiv x_a - x_b$ and $\Delta y \equiv y_a - y_b$. After time-averaging we obtain

$$\begin{aligned} \langle V_a(t) \star V_b(t) \rangle &= \int_{l,m} \langle |A(l, m)|^2 \rangle e^{2\pi i(\Delta xl + \Delta ym)} dl dm \\ &= \int_{l,m} I(l, m) e^{2\pi i(u l + v m)} dl dm \\ &= \mathcal{F}\{I(l, m)\}, \end{aligned} \quad (10)$$

where $\Delta x = u$, $\Delta y = v$ and $I(l, m) = \langle |A(l, m)|^2 \rangle$ (chap. 3 of Thompson et al., 2001; Vanderlinde, 2017).

Equation 10 shows the Fourier transform connection between the cross-correlation and the intensity map $I(l, m)$. The intensity map is therefore obtained by performing

an inverse 2D Fourier transform on the visibilities which is of course limited by how well the visibilities have been measured. A single pair of antennae samples a single (u, v) point in visibility space, meaning that the more baselines there are in the array the better the uv -coverage and the more accurate the final map is. The uv -coverage is also greatly improved by the rotation of the Earth since different orientations relative to the object change the (u, v) coordinates (Thompson et al., 2001). Images formed from poorly sampled visibilities will result in a large number of periodic ‘blobs’ or ‘stripes’ that are not real and are purely a side-effect of the periodic functions used to perform the Fourier transform.

To obtain maps at different frequencies the signal must be binned into different spectral channels before being correlated. To obtain maps of specific polarizations in addition to different frequencies, either receivers sensitive to different polarizations must be used (like at ALMA) or the observing time is split so that the receivers are exposed to light of different polarization states. The SMA does the latter strategy and uses a quarter-wave plate (QWP) in the beam of each antenna to sample the two polarization states: left-CP (LCP) and right-CP (RCP). Each antenna can only sample one polarization state at a time, and the QWP is rotated 90° to sample the other state. To obtain full polarimetric information for the visibilities from a single baseline, the two antenna must correlate their responses to every combination of polarization state. That is, if an antenna can sample polarization states ‘ L ’ and ‘ R ’ (which corresponds to 90° rotations of the QWP), then, for a pair of antennae, four correlations must be found: LL , LR , RL , and RR . On the SMA this is done by rotating the QWPs on both antennae in a cycle that repeats every 4-6 minutes (Marrone et al., 2008). Figure 2 shows the SMA’s QWP.

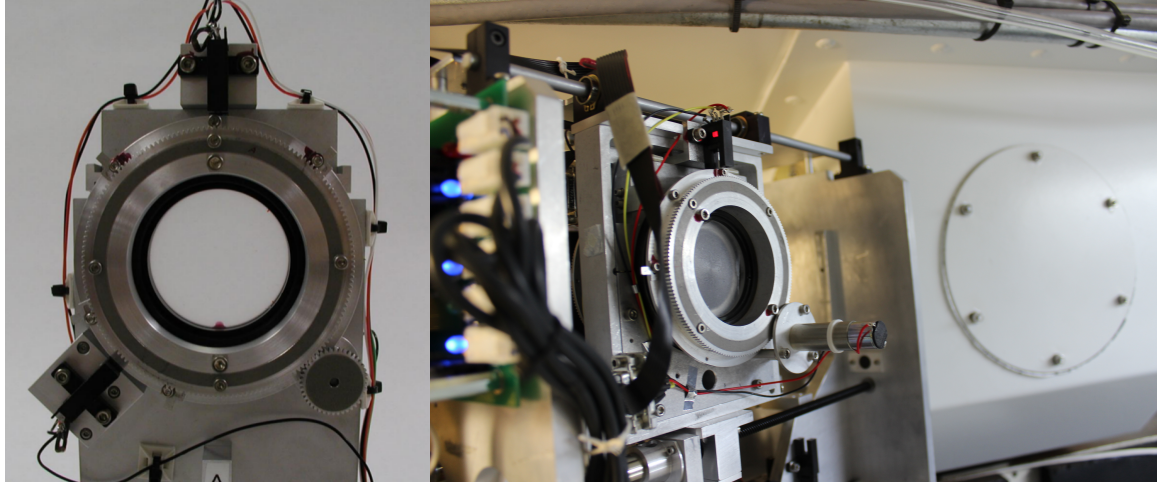


Figure 2: (*left*) The SMA’s quarter-wave plate (QWP) mounted on a rotation stage. Optical brakes (top and bottom left) determine the position of the QWP. Adjustable flags (small screws on perimeter of the rotation stage) at $\pm 45^\circ$ from the top optical brake set the positions of the waveplate (from Fig. 1 of Marrone et al., 2008). (*right*) The QWP mounted inside the cabin of an SMA antenna in the path of the beam (personal photo).

2.2 Data Reduction with *Miriad*

The data reduction package *Miriad* (Sault et al., 1995) implements and performs most of the required computational tasks for calibrating the data and performing the inverse Fourier transform to obtain maps. When observations are taken their brightness is usually calibrated against measurements of quasars that are taken during the same night, since the quasars used are assumed to be steady, bright, unchanging sources. The data presented in this paper were already calibrated by Dr. Rao and Dr. Girart, and so the calibration process will not be explained in detail here. The calibration involves calculating gain coefficients to correctly scale the visibilities to their true intensities. In *Miriad*, programs that perform useful operations on the data are broken up into commands called ‘tasks’ that can be scripted using bash scripts or Python. This section will summarize the most important tasks for creating images from the visibilities.

The `invert` task performs a standard two-dimensional fast Fourier transform

(FFT) on a grid whose size can be specified by the user. It also generates a beam map that gives the response of the interferometer to a point source based on the location of the antennae in the array and the frequency being observed. The beam map is necessary because `invert` alone tends to produce maps of objects that are filled with sidelobes: bumps and peaks and stripes that arise in the map when the *uv*-coverage of the array is irregular. In interferometry the *uv*-coverage is often irregular due to the fact that the placement of dishes is limited to the geography of the region (like on Mauna Kea for the SMA) and specific dishes often need to be excluded from the data due to malfunction. The beam map, because it is made with observations of a point source, can tell us what exactly the pattern of sidelobes is and makes it possible to deconvolve the sidelobe pattern from the dirty map, leaving behind the real structure. The process for doing this is called Högbom iteration (Högbom, 1974) or ‘CLEAN’ and is implemented by the `clean` task in *Miriad*.

The `clean`*ing of the dirty map is performed by subtracting the entire dirty beam from the position where the dirty map is maximum. The amplitude of the dirty beam is usually normalized to be a fraction of the maximum of the dirty map, called the loop gain. This subtraction is repeated on what remains of the map until nothing is left. A model is then built by placing point sources at all the positions where a peak was removed at the corresponding amplitude that it was removed at. By then analytically calculating a “clean” beam, which is the response to a point source given the diameter of a dish, the model can be convolved with the clean beam using the `restor` task to obtain a clean map. Figure 3 demonstrates the `clean`-ing process on the IRC+10216 data presented in the attached paper. Note that the CLEAN algorithm works on extended sources like nebulae or molecular clouds essentially by modelling them as a collection of point sources.

* `selfcal` -> used to adjust the gain coefficients by doing jacobi iteration (maybe leave this out?), equation from paper

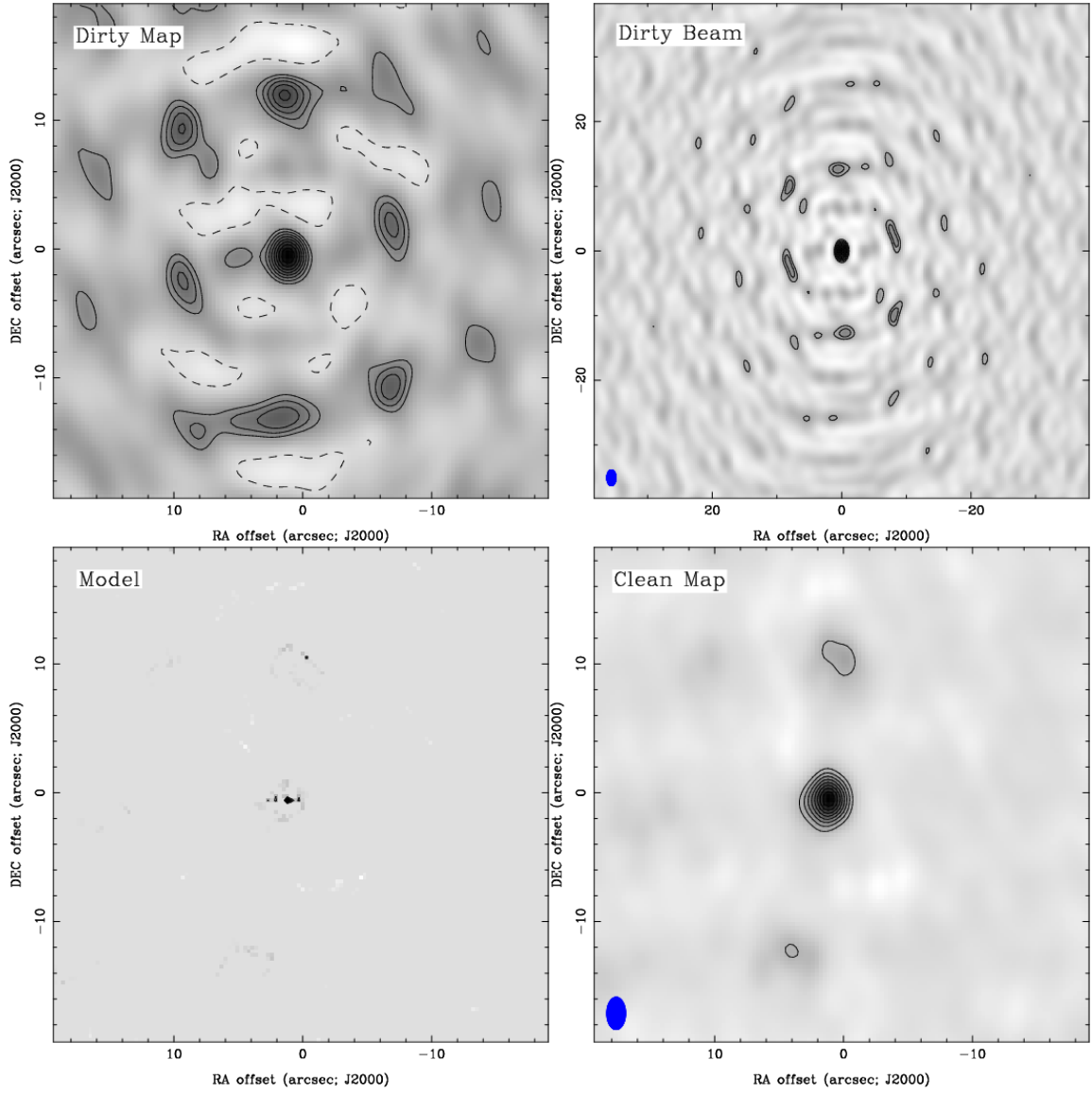


Figure 3: The dirty map (**top left**), dirty beam (**top right**), model obtained from the clean task (**bottom left**), and deconvolved CLEAN map of IRC+10216 (**bottom right**). Contour levels are at -20%, 20%, 30%, 40%, etc. of the maximum. Pixels show the same data, darker pixels represent higher intensity. Notice the six peaks around the larger central peak in the dirty map are also present in the dirty beam and are largely absent in the clean map.

Another task critical to the results presented in the paper is `selfcal` (self-calibration), which makes additional corrections to the gain calibration of the data. As explained in the paper this is necessary to correct the very small offset between beams of different polarizations that leads to false Stokes V signals. The `selfcal` task takes the clean model found from `invert-ing` and `clean-ing` the initial visibilities and uses it to find new gain coefficients that better fit the model. The gain coefficients can be further improved by repeating the self-calibration process on a new model generated from the last gain coefficients to be found. The gain coefficients (which are complex-valued) are searched for and found iteratively by minimizing the following error heuristic:

$$\epsilon^2 = \sum |\mathcal{V}_{ij} - g_i g_j^* \hat{\mathcal{V}}_{ij}|^2, \quad (11)$$

where \mathcal{V}_{ij} are the measured visibilities found by correlating signals from antenna i and j , $\hat{\mathcal{V}}_{ij}$ are the model visibilities for the same baseline, and g_x are the complex gain coefficients. By finding the gain coefficients that minimize eq. (11), `selfcal` adjusts the measured visibilities until they match the model, and, when models are regenerated after each iteration of `selfcal`, the gain coefficients eventually converge and further iterations do not improve the image (Schwab, 1980; Sault et al., 2008). The self-calibration process can also be applied on visibilities with different polarizations, which is what allows us to correct the offset in each polarized beam.

While *Miriad*'s tasks make it easy to create scripts to automate data reduction and correct the data, the tasks themselves take parameters that must be manually found based on the data set being used, and are usually different across different objects. Using *Miriad* to search the data was initially a monumental challenge since our archive search started with over 25 different sets of data of different celestial objects taken with different spectral configurations. For example, an early step in the `invert-ing` process is to average the spectral channels that make up a spectral line (like CO ($J = 3 \rightarrow 2$) at 345.8GHz) so that the inversion process completes

successfully. This is done by specifying the number of channels to end with after averaging, the velocity (in km/s) of the channel to start averaging at, and the number of channels to merge together. This involved manually opening the spectra of interest, counting the correct number of channels to cover the entire line, and then switching the x-axis of the displayed spectra to find the corresponding velocity of the starting channel. This is then passed to the `invert` task like so:

```
1 invert line=vel,18,-43,2,2 vis=[...]
```

where the format is `line=vel,{# of channels},{starting channel},{step},{# to merge}`. The `invert` task has a bug where if the step size does not agree with a hidden rule I was unable to ascertain, it would fail, requiring you to increase the step size and manually recount the number of channels to input as the first number. Since each dataset required a correction script to be written for it, and we wanted to search as much data as possible, inefficiencies like the example above quickly made progress difficult and cumbersome.

To improve the workflow and automate little menial details like counting it was necessary to automate parameter generation for *Miriad*'s tasks. In a language like bash, which *Miriad* supported scripting for natively, such automation would bring its own cumbersome details, and it became clear a language like Python would be better suited for the task. No Python wrapper existed for *Miriad* so I created one and used it to generate any tedious parameters needed for any of the *Miriad* tasks, including detecting when `invert` fails due to the mysterious step bug and automatically changing the step size until the task completes. Other notable features include dumping spectral information to the terminal and parsing it in Python for information needed to generate other parameters, counting channels automatically, displaying a window with a spectrum that outputs channel information on mouse click, and, in general, allowing one to take advantage of the language features of Python such as loop structures, function definitions, and string substitution. For example, the Python method

used to automate the line selection parameter for `invert` is the following:

```
1 def averageVelocityLine(vis, factor):
2     velrange = getVelocityRange(vis)
3     nvels = round(abs(velrange[0] - velrange[1])/factor)
4     startvel = round(velrange[1])
5     return 'vel,{0},{1},{2},{2}'.format(nvels, startvel, factor)
```

which, under the hood, gets the velocity range of the line by using the output of the `uvlist` task in *Miriad* and parsing it for the velocity range before using it to compute the necessary number of channels and building the necessary string in the format that *Miriad* expects.

The Python *Miriad* wrapper works by generating the necessary bash command to run and then passing the command to the terminal. Depending on the task, the output can be displayed in the terminal as usual or can be intercepted by Python and used for other tasks.

Having a Python interface to *Miriad* also made it possible to connect the data to the plotting utilities available in Python, such as `matplotlib`, and also allowed easier access to *Miriad*'s own plotting utilities like `cgdisp` which is used to display contour plots of the maps.

Creating an automation suite for *Miriad* in Python and connecting it directly to several different custom plotting methods made it possible to correct more data, find potential Stokes V signals across different spectral lines more efficiently, and create the many figures and maps required to convince ourselves of whether the signals were real or not.

2.3 Code Repositories

All the code that performs the data reduction, squint correction, and plotting is available online.

The data analysis and correction scripts can be found at github.com/mef51/SMAData. This repository contains all the archival polarimetric data from the SMA (minus the

actual data, scripts only). The folders relevant to the attached paper are `IRC+10216/`, `080106_Ram_Spectra/` (for Orion KL), `141028_ngc7538/` (for NGC7538), and `101014_NGC1333_Ram/` (for NGC1333).

Within that repository is the `squintscripts/` folder which contains all the scripts for generating the figures included the paper as well as some extra figures. The `paperplots.py` file contains some utilities. The `GetCOMMaps.py` file generates all the maps used in the paper. `CompareImageSpectra.py` generates the large before-and-after correction comparison of the spectra (Figure 4 of the attached paper).

The Python wrapper for *Miriad* described in the previous section lives in its own repository due to its potential use for others and can be found at github.com/mef51/smautils. It contains the wrapper as well as a library (`squint.py`) for performing the squint correction detailed in the paper. It is published on the Python Package Index (PyPi) and can be installed by anyone by running the command ‘`pip install smautils`’ on the terminal.

3 Acknowledgements

I’d like to thank my supervisor Martin Houde for his advice and guidance during the last year and for sending me to Hilo, Hawaii for two weeks as soon as I finished my classes despite my having only a vague idea of what my project would entail and exactly zero research experience in Astronomy. Baptism by fire works.

I’m also grateful to Ramprasad Rao and Josep Miquel Girart who not only made my visit to Hilo productive but also warm and fun. Thank you Josep Miquel for not letting me drive up Mauna Kea on my own the night before our respective flights.

I’m grateful to my friends, roommates, and the rock climbing crew for giving me things to do that are happily unrelated to work.

4 References

- Chandrasekhar, S., & Fermi, E. 1953 ApJ, 118, 113
- Cortes, P. C., Crutcher, R. M. & Watson, W. D. 2005, ApJ, 628, 780.
- Cotton, W. D., Ragland, S., & Danchi, W. C. 2011, ApJ, 736, 96
- Crutcher, R. M. 2012 Annu. Rev. Astron. Astrophys, 50, 29-63
- Davis, L., Jr. 1951, PhRv, 81, 890
- Girart, J. M., Crutcher, R. M. & Rao, R. 1999, ApJ, 525, L109.
- Girart, J. M., Rao, R., Marrone, D. P. 2006 Science, 313, 5788, 812-814
- Girart, J. M., Patel, N., Vlemmings, W. H. T., & Rao, R. 2012, ApJ, 751, L20.
- Glenn, J., Walker, C. K., Bieging, J. H., et al. 1997, ApJ, 487, L89.
- Goldreich, P., Kylafis, N. D. 1981 ApJ, 243, L75-L78
- Greaves, J. S., Holland, W. S., Friberg, P., et al. 1999, ApJ, 512, L139.
- Hamaker, J. P., Bregman, J. D., & Sault, R. J. 1996 A&A Suppl. Ser., 117, 137-147
- Hezareh, T., & Houde, M. 2010, PASP, 122, 786
- Hezareh, T. J., Wiesemeyer, H., Houde, M., Gusdorf, A., Siringo, G. 2013 A&A, 558, A45
- Hildebrand, R. G., Kirby, L., Dotson, J. L., Houde, M., Vaillancourt, J. E. 2009 ApJ, 696, 567-573
- Högbom, J. A. 1974 Astron. Astrophys. Suppl., 15, 417-426
- Houde, M., Vaillancourt, J. E., Hildebrand, R. H., Chitsazzadeh, S., & Kirby, L., 2009 ApJ, 706, 1504

- Houde, M., Hezareh, T., Jones, S., & Rajabi, F. 2013 ApJ, 764, 24
- Houde, M. 2014 ApJ, 795, 27
- Hull, C. L. H., Plambeck, R. L., Kwon, W., Bower, G. C., Carpenter, J. M., Crutcher, R. M., et al. 2014, ApJ Suppl., 213, 13
- Lai, S.-P., Girart, J. M. & Crutcher, R. M. 2003, ApJ, 598, 392.
- Muñoz, D. J., Marrone, D. P., Moran, J. M., & Rao, R. 2012 ApJ, 745, 115
- Marrone, D. P. & Rao, R. 2008, Proc. SPIE 7020, 70202B
- Nakano, T., Nakamura, T. 1978 Publ. Astron. Soc. Japan 30, 671-679
- Sault, R. J., Teuben, P. J. & Wright M. C. H. 1995 ADASS IV, ASP Conference Series, 77, 433-436
- Sault, R. J., Hamaker, J. P., & Bregman, J., D. 1996 A&A Suppl. Ser., 117, 149-159
- Sault, R. J., Killeen, N. 2008, Miriad Users Guide, Australia Telescope National Facility
- Schwab, F. R. 1980, Proc. SPIE 0231, Intl Optical Computing Conf I
- Tang, Y.-W., Ho, P. T. P., Koch, P. M., & Rao, R. 2010, ApJ, 717, 1262.
- Thompson, A. R., Moran, J. M., & Swenson Jr, G. W. 2001, Interferometry and synthesis in radio astronomy (John Wiley & Sons)
- Vanderlinde, K. “Radio Telescope Fundamentals”, slide show presentation, Dunlap Summer School, July 2017